Coexistence of Equatorial Coupled Modes of ENSO*

LUIS BEJARANO

Geophysical Fluid Dynamics Institute, The Florida State University, Tallahassee, Florida

FEI-FEI JIN

Department of Meteorology, University of Hawaii at Manoa, Honolulu, Hawaii

(Manuscript received 14 September 2006, in final form 20 June 2007)

ABSTRACT

To study the regimes of leading ocean–atmosphere coupled modes of relevance to the El Niño–Southern Oscillation (ENSO) phenomenon, a comprehensive eigenmode analysis of an intermediate coupled model linearized with respect to an array of basic states is performed. Different kinds of leading modes are found to coexist and become unstable under wide ranges of basic states and parameter conditions. In particular, the two most important modes have periods of around 4 and 2 yr. They are referred to as the quasi-quadrennial (QQ) and the quasi-biennial (QB) modes, respectively. The positive coupled feedback destabilizes and quantizes the near-continuous spectrum for the low-frequency modes of the upper-ocean dynamics, giving rise to these leading modes with distinct periodicities. The primary mechanism for the phase transition of the QQ mode is due to the slow oceanic dynamic adjustment of equatorial heat content, which is consistent with the simple conceptual recharge oscillator, whereas anomalous advection of sea surface temperature by equatorial zonal current anomalies plays a dominant role in the phase transition of the QB mode. The coexistence of these ENSO-like coupled modes under the present climate conditions may provide an explanation for the observed rich variations in ENSO behaviors.

1. Introduction

Major progress in understanding and modeling the coupled ocean–atmosphere interaction in the Tropics and the salient features of the El Niño–Southern Oscillation (ENSO) phenomenon has been made in the past two decades (Bjerknes 1969; Rasmusson and Carpenter 1982; Philander et al. 1984; Cane 1984; Cane and Zebiak 1985; Schopf and Suarez 1988; Battisti and Hirst 1989; Philander 1990; Neelin et al. 1994; Jin 1996, 1997a,b; Weisberg and Wang 1997; Wallace et al. 1998; McPhaden et al. 1998; Neelin et al. 1998; Wang and Picaut 2004). Decades of research on the ENSO dynamics have led to the basic understanding of ENSO as a natural oscillator (Suarez and Schopf 1988; Battisti and Hirst 1989; Jin 1996, 1997a,b). The positive coupled ocean–atmosphere feedback tends to sustain the sea surface temperature (SST anomalies whereas, following each major El Niño or La Niña event, the upper-ocean heat content discharge and recharge, which serve as delayed restoring mechanisms, are responsible for the back-and-forth oscillation between El Niño and La Niña events, much like a swing.

This simplistic view of ENSO, which appeared to have provided a reasonable framework for understanding some of the ENSO behaviors observed in modern times and simulated in different models, is only partially consistent with the observations. In addition to the main 3–5-yr cycle of ENSO, interannual coupled modes of variability of different time scales have been noted (e.g., Zhang et al. 1997; Jiang et al. 1995; Jin et al. 2003). For instance, it has been recently suggested that there is a near-annual coupled mode (Jin et al. 2003; Tozuka and Yamagata 2003). This fast mode, with a period of about 12–18 months, was assumed to be superimposed on the slow 3–5-yr cycles of ENSO, and it appears to be independent of the slow ENSO mode. A

* School of Ocean and Earth Science and Technology Contribution Number 7136 and The Florida State University Geophysical Fluid Dynamics Institute Contribution Number 453.

Corresponding author address: Dr. Fei-Fei Jin, Department of Meteorology, University of Hawaii at Manoa, 2525 Correa Road, HIG 350, Honolulu, HI 96822.
E-mail: jff@soest.hawaii.edu

DOI: 10.1175/2007JCLI1679.1

number of studies were also directed to identify physical mechanisms for the so-called tropical quasi-biennial oscillation (TBO), which was suggested to involve ocean–atmosphere interaction in the tropical Pacific and Indian Oceans and the monsoon system (e.g., Meehl 1994, 1997; Li et al. 2001). Toward the lower-frequency end, it has been recognized that there are significant decadal–interdecadal variations in the tropical Pacific. This decadal–interdecadal variability has broad spatial patterns in the atmospheric circulation and SST anomalies over the Pacific Ocean (Trenberth and Hurrell 1994; Deser and Blackmon 1995; Deser et al. 1996; Zhang et al. 1997; Miller et al. 1998; Latif 1998). Several different hypotheses about the origin of the decadal variability have been put forward (Latif and Barnett 1994; Jin 1997c; Gu and Philander 1997; Kleeman et al. 1999; Barnett et al. 1999; Jin et al. 2001; Schneider 2000). It is still unclear whether the observed variability on different time scales can be really attributed to physically independent coupled modes of the tropical Pacific climate system.

As a null hypothesis, the tropical Pacific variability of the time scales other than the main ENSO time scale may be simply regarded as a part of the red noise generated, for instance, by stochastic forcing. However, results from both observational and modeling studies indicate that this may not be the case necessarily. The possibility of the coexistence of different coupled modes in the coupled tropical ocean–atmosphere system was, in fact, found in a number of coupled models. For instance, in the Zebiak and Cane (1987, hereafter ZC) model, in addition to the nearly 4-yr ENSO mode, there is another independent fast mode called the "mobile" mode, with a period of about 9–10 months (Zebiak 1984). A fast mode of about 6 months was clearly present, together with a slow ENSO-like mode in more complex models (Neelin 1990; Philander et al. 1992).

In another recent study (Wang et al. 2003a,b) in an idealized coupled tropical ocean–atmosphere model, it was found that some of the very low-frequency modes of tropical ocean dynamics (Jin 2001b) developed into two leading coupled modes, including an ENSO-like mode and another coupled decadal mode. It was suggested that these two kinds of coupled modes generated by the tropical coupled dynamics could be responsible for both the dominant interannual and decadal variability. Moreover, the existence of different regimes for different modes has been suggested in the studies with theoretical models (e.g., Hirst 1986; Jin and Neelin 1993a,b; Neelin and Jin 1993, hereafter JN93; Fedorov and Philander 2000, 2001, hereafter FP01).

The objective of this study is to demonstrate that independent coupled modes may contribute to ENSO-related variability by extending the earlier work by JN93 and FP01 through an extensive stability analysis of an intermediate coupled ocean–atmosphere model under various simulated climate conditions in the tropical Pacific. Unlike the previous work by JN93 and FP01, who employed the stripped-down version of the ZC model, this study uses the *full* ZC model to perform the stability analysis.

The remainder of this paper is organized as follows. Sections 2 and 3 describe the construction and linearization of the coupled ocean–atmosphere model. Section 4 follows with an extensive linear stability analysis of the coupled model under many different background states. Section 5 presents a heat budget analysis for the most unstable modes. Nonlinear integrations of the model are discussed in section 6. Section 7 summarizes the results.

2. Model description

Although complex coupled ocean–atmosphere models are available today for ENSO modeling, the tool chosen in this study is an intermediate coupled model of the ZC type. As in all coupled models, some aspects of the simulated ENSO of the ZC model do not fully agree with the observations (Perigaud and Dewitte 1996). Nevertheless, the ZC model does successfully reproduce, at least qualitatively, the major features of the ENSO cycle. Furthermore, the *full* ZC model is a natural extension of the earlier theoretical studies by JN93 and FP01, who used the stripped-down version of the ZC model, an approximation that introduces a strong constraint because of the artificial specification of the meridional structure of the SST pattern.

The atmospheric component of the model is exactly the same as that of ZC, which follows Gill's (1980) framework. The ocean component of the model is a linear, reduced-gravity model on the equatorial beta plane with longwave approximation. To reduce the degrees of freedom in this modified version of the ZC model (MZC), the ocean currents, the thermocline depth, and the atmospheric wind stress are expanded in Hermite functions following Battisti (1988). A standard truncation that includes the Kelvin mode and the first 30 Rossby modes is used, with finite differencing of the wave equations in the x direction on a 5.2° grid (30 points). A full description of the governing equations in the model can be found in the appendix of ZC.

The original ZC model and our MZC version differ in the following four aspects:

1) Different meridional discretization is adopted in the MZC model. Here the dynamical fields are ex-

panded in Hermite functions following Battisti (1988).

2) The zonal resolutions of the wave equations and SST equation are reduced to the same 5.2° grid, whereas in the meridional direction the discretization of the SST equation follows that of the original version of ZC. This change provides an extra reduction of the degrees of freedom of the coupled model.
3) The truncation error and the coarse grid for the ocean waves give rise to some additional numerical damping. As a rough compensation, the weak linear damping used in the ocean momentum and continuity equations is set to zero.
4) Finally, the Heaviside function in the ZC formulation is replaced by a smoother function, defined as $M(x) = 0.5x[\tanh(x/a) + 1]$. A small value of a is chosen to ensure that the hyperbolic tangent function approaches the Heaviside function used in the original ZC formulation

Everything else in the MZC model remains the same as the original version of the ZC model, including all the physical parameters, the interpolation schemes, the spatial domain, and the time stepping. The testing of the MZC model for the standard parameters and basic state of the ZC model showed that the interannual variability displayed by both models presents negligible differences (Bejarano 2006).

3. Linearizing the model

a. Basic states

To investigate the sensitivity of coupled modes in the MZC model to different basic states, an array of basic states is constructed. Each basic state includes longitude–latitude distributions of SST, oceanic surface currents, upwelling, and longitudinal distribution of the mean thermocline depth, which are all independent of time. These basic states are constructed by following the similar approach taken by FP01, in which two control parameters, denoted as a_H and a_W, are used to alter the reference upper-layer thickness $H_0 = a_H H_C$, and the mean wind stress $(\bar{\tau}^X, \bar{\tau}^Y) = a_W(\bar{\tau}^X_C, \bar{\tau}^Y_C)$. Here $(\bar{\tau}^X_C, \bar{\tau}^Y_C)$ denotes the observed climatological mean wind stress, and $H_C = 150$ m is the standard value for the reference upper-layer thickness.

The values of a_H and a_W are varied so that the wind stress $(\bar{\tau}^X, \bar{\tau}^Y)$ varies from 80% to 120% ($0.8 \le a_W \le 1.2$) of its observed intensity, with an increment of 1%, and the reference upper-layer thickness alters from 130 to 160 m, with an increment of 1 m. With each pair of specified a_H and a_W, the ocean component of the ZC model is integrated to reach its steady-state solution.

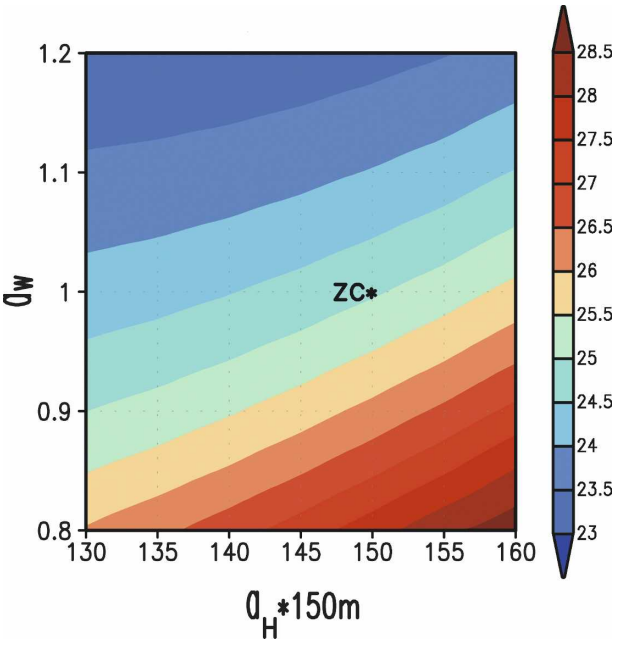

FIG. 1. Temperature (°C) of the basic state averaged over the eastern tropical Pacific Ocean (5°S–5°N, 90° to 160°W) as a function of a_W and a_H. The point marked as ZC represents the standard mean basic state of the ZC model ($a_H = 1$, $a_W = 1$).

The difference between the solution for each specific set of (a_H, a_W) and the solution for $a_H = 1$ and $a_W = 1$ is denoted as $\Delta\bar{T}$, $\Delta\bar{\mathbf{u}}_1$, $\Delta\bar{w}_S$, and $\Delta\bar{h}$. The procedure is repeated for all different pairs of a_H and a_W. Then, the array of the basic states in the MZC model is defined as follows:

$$\bar{T} = \bar{T}_C + \Delta\bar{T}, \quad \bar{\mathbf{u}}_1 = \bar{\mathbf{u}}_{1C} + \Delta\bar{\mathbf{u}}_1,$$
$$\bar{w}_s = \bar{w}_{sC} + \Delta\bar{w}_s, \quad \text{and} \quad \bar{h} = \bar{h}_C + \Delta\bar{h}. \tag{1}$$

Here, $\bar{T}_C$, $\bar{\mathbf{u}}_{1C}$, $\bar{w}_{sC}$, and $\bar{h}_C$, denote the basic-state variables in the original ZC model. To be consistent with the basic state in the ZC model, $\Delta\bar{h}$ is set to its equatorial values so that $\bar{h}$ remains independent of latitudes.

A total of 1271 different basic states are constructed to vary continuously in the two-dimensional parameter space (a_H, a_W) around the reference basic state of the MZC model, as labeled by ZC in Fig. 1 at the point ($a_H = 1$, $a_W = 1$). These nearly continuous changes are dynamically consistent. For instance, toward the lower-right (upper left) corner of the two-dimensional parameter space, corresponding to basic states with deeper reference upper-layer thickness and weaker mean wind stress, the temperature in the eastern Pacific is relatively warm (cold) and the thermocline is deep (shallow).

b. Linearization

The linearization process of the model depends on the basic state and the model physical parameters, denoted as **P**. Thus, for a predetermined basic state and a specified **P**, the nonlinear MZC model can be written, symbolically, as

$$\frac{d\mathbf{X}_T}{dt} = F[\mathbf{X}_T, \mathbf{X}_q, \mathbf{X}_\tau, \overline{\mathbf{X}}(a_H, a_W), \mathbf{P}],$$

$$\frac{d\mathbf{X}_q}{dt} = L(\mathbf{X}_q, \mathbf{X}_\tau, a_H),$$

$$\mathbf{X}_\tau = \mathbf{A}\mathbf{X}_T,$$

$$\mathbf{X}_T = [T(i, j, t), \quad i = 1, \ldots 18, \quad j = 1, \ldots 30], \quad \text{and}$$

$$\mathbf{X}_q = [q(n, j, t), \quad n = 1, \ldots 31, \quad j = 1, \ldots 29], \qquad (2)$$

where $\mathbf{X}_T$ is the vector for the SST anomalies on all the grid points of the model, $\mathbf{X}_q$ is the vector for the anomalies of the Kelvin wave and the 30 Rossby waves at all zonal grid points, and $\mathbf{X}_\tau$ is a vector that contains the zonal and meridional wind stress anomalies at all grid points. The wind stress vector is linearly related to the SST anomaly field through the matrix **A**. This linear relation may be derived numerically from the atmosphere component of the MZC model by solving all of the steady responses for a small SST anomaly assigned to each grid point. The vector $\overline{\mathbf{X}}(a_H, a_W)$ denotes the particular basic state of the MZC model, which is a function of the parameters a_H and a_W. It should be noted that when a_H changes, it not only alters the features in the basic state, which will impact the stability of the system, but it also alters the equatorial ocean wave speed and thus has a direct impact on the time scale of the ocean dynamics.

The linear version of Eq. (2) can be written as

$$\frac{d\mathbf{X}(t)}{dt} = \mathbf{M}[\overline{\mathbf{X}}(a_H, a_W), \mathbf{P}]\mathbf{X}(t), \qquad (3)$$

where $\mathbf{X}(t)$ represents the whole state vector, which includes the ocean wave components $\mathbf{X}_q$ and the SST components $\mathbf{X}_T$. This state vector has a dimension of 1439 (e.g., 899 ocean wave components plus 540 SST components) under the chosen model resolution. The Jacobian matrix $\mathbf{M}[\overline{\mathbf{X}}(a_H, a_W), \mathbf{P}]$is obtained by linearizing the MZC model equations with respect to the mean basic state $\overline{\mathbf{X}}(a_H, a_W)$. It should be noted that although each of the 31 wave components has 30 grid points in the zonal direction, they only amount to 29 prognostic equations, because each has a diagnostic wave-reflection boundary condition. The SST anomaly field has a total of 540 prognostic equations on the 540 grid points.

4. Stability analysis

a. Stability diagrams

To analyze the dependence of the eigenvalues of the MZC model linearized with respect to the nearly continuous set of basic states, we set the physical parameters **P** as the same as those chosen in the ZC model, except that we consider two different values for the entrainment efficiency factor γ. The standard value of γ chosen in the ZC model is 0.75. This parameter, which measures the effectiveness of the anomalous vertical advection of anomalous subsurface water and thus the so-called thermocline feedback (cf. An and Jin 2001), is one of the crucial and uncertain parameters in the ZC model. A reduced value at $\gamma = 0.5$ is also considered in this analysis to examine the robustness of stability regimes under different choices of this parameter.

Following JN93, we illustrate the emergence of the leading coupled modes and their dependence on a particular parameter by plotting all of the eigenvalues of the linear model for each different value of the parameter that varies continuously in a reasonable range. For example, as shown in Fig. 2 for the case of $\gamma = 0.5$ and $a_H = 140/150$, we overlay all of the eigenvalues corresponding to 41 different choices of a_W from 0.8 to 1.2, varying with an increment of 1%. This range of a_W corresponds to 41 different basic states with mean wind forcing varying sequentially from 80% to 120% of its standard observed intensity.

Because the linearization of the model with respect to each basic state produces 1439 eigenvalues, the collective plot shown in Fig. 2a has 58 999 eigenvalues. Among all of the 58 999 eigenvalues, there are only two branches that stand out and become unstable modes, whereas the remaining eigenvalues are all damped modes. It should be pointed out that the complex conjugate of each complex eigenvalue is plotted in Figs. 2a,b as well; that is why these plots are symmetric with respect to the frequency axis. A complex eigenvalue and its complex conjugate just account for one oscillatory mode. The coexistence of at least two outstanding oscillatory modes of distinct periods is illustrated clearly in the zoomed-in picture shown in Fig. 2c.

It is noted that, on these branches, the periods as well as the growth rates are continuous functions of the parameter a_W, as shown in Figs. 2d,e. As seen in Fig. 2d, the one branch represents a mode with a period of about 3.3–5.5 yr, whereas the other branch has a period of about 1.5–2 yr. We will refer to these as the quasi-quadrennial (QQ) and the quasi-biennial (QB) modes, respectively, according to the different ranges of their frequencies. The periods of the QQ and QB modes are

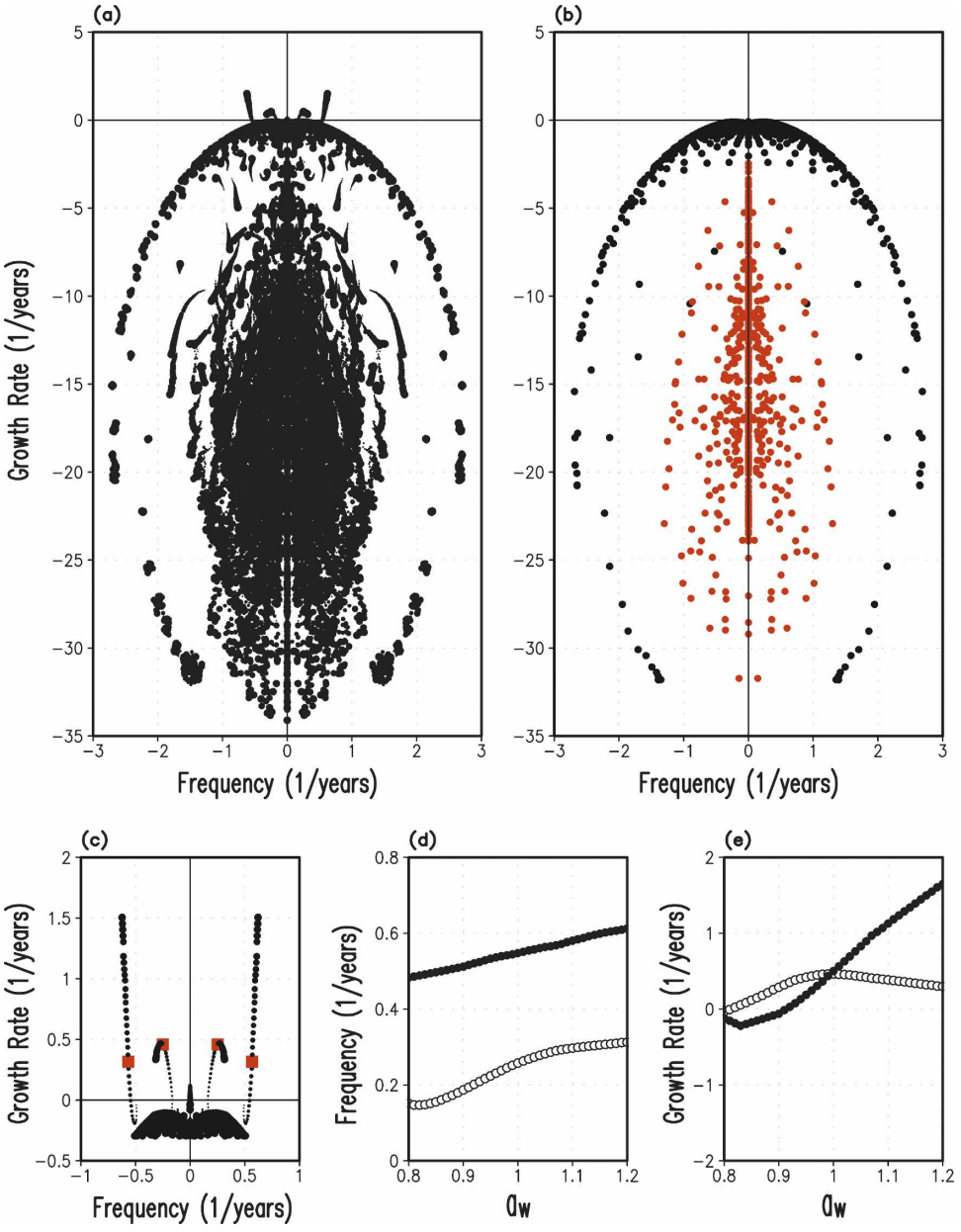

FIG. 2. (a) Collective plot of eigenvalues of the linearized MZC ENSO model for the 41 basic states resulting from setting the reference upper-layer thickness to 140 m and sequentially varying the mean wind stress from 80% to 120% of its observed intensity with an increment of 1%. The size of each pair of dots increases as a_W increases. (b) Collective plot of the eigenvalues of the linearized MZC ENSO model for the uncoupled case for ($a_H = 1$, $a_W = 1$); the red (black) dots correspond to the uncoupled SST (ocean dynamics) modes. (c) A portion of the upper part of (a) for a clear view of the leading braches of modes of QQ and QB periodicities. Red squares in this panel denote the eigenvalues of the two leading modes under a basic state defined by ($a_H = 140/150$, $a_W = 1$). The (d) frequencies and (e) growth rates of the two leading modes in (c) as functions of a_W are also shown.

not very sensitive to different basic states following changes of a_W. The QQ mode is mostly unstable, unless a_W is close to 0.8, whereas the growth rate of the QB mode increases rapidly with a_W; the QB mode becomes the leading unstable mode under the basic states with a stronger mean wind and thus a colder mean cold tongue SST.

As noted in Wang et al. (2003a,b), the coupled QQ and QB modes are connected to the low-frequency part of ocean dynamic spectrum. To support this argument,

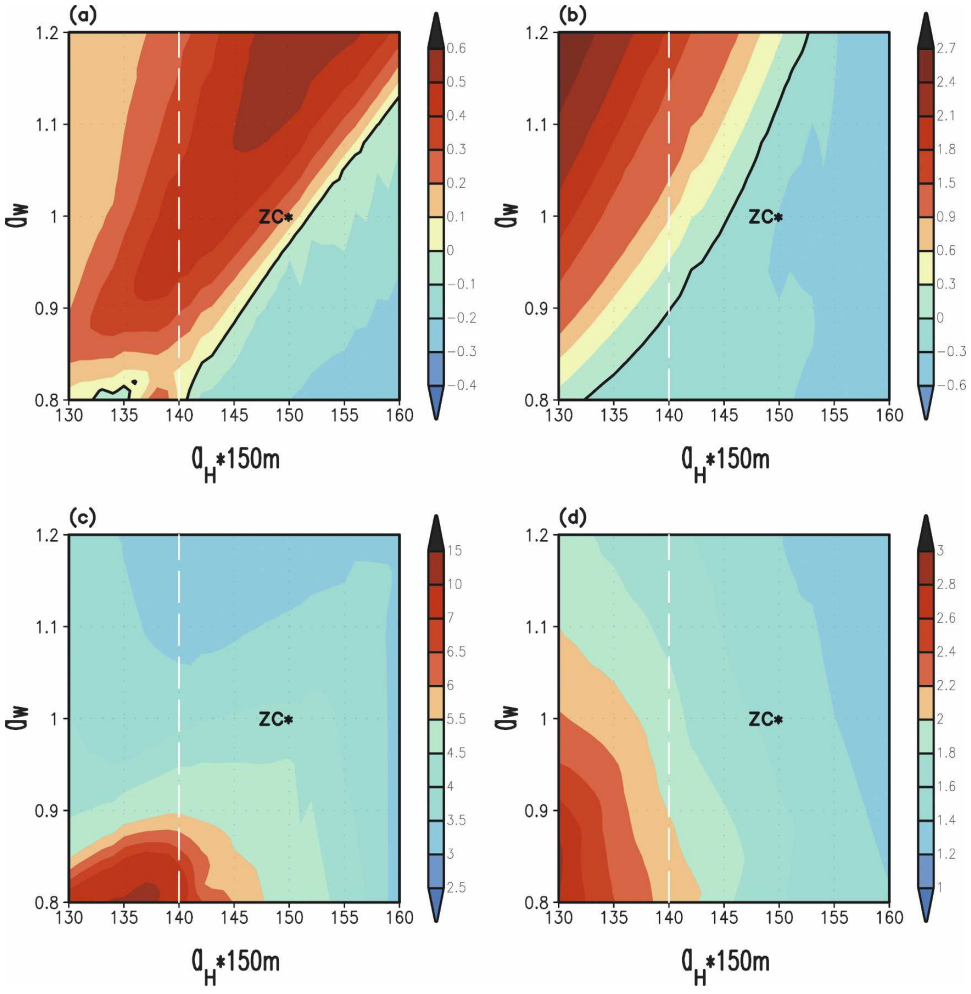

FIG. 3. Changes in (a) the growth rate (yr^{-1}) and (c) period (yr) of the QQ mode as a function of a_W and a_H. (b), (d) Same as (a), (c), respectively, but for the QB mode. The point marked by ZC represents the point of standard parameter setting of the original ZC model. The growth rates and periods of the QQ and QB modes along the white dashed line are those in Fig. 2c. The zero growth rate is shown by black contours in the upper panels.

a collective plot including the uncoupled SST modes (red dots) and ocean dynamics modes (black dots) is shown in Fig. 2b. The uncoupled SST modes are heavily damped, whereas the low-frequency uncoupled ocean dynamics modes (Jin 2001) are less damped. The two outstanding branches in Fig. 2c are connected with the uncoupled ocean dynamics spectrum. These outstanding and distinct leading coupled modes result from the positive Bjerknes coupled feedback that destabilizes and quantizes the near continuum of uncoupled modes.

As in FP01, we further examine the dependence of the periods and the growth rates of the leading QQ and QB modes on the two-parameter space for the entire array of the basic states. As shown in Fig. 3, the results in Fig. 2c correspond to the cross section along the vertical line. The point denoted by ZC on the diagrams shows that the QQ mode is unstable and QB is damped under the original ZC basic state. The growth-rate diagrams indicate that over the upper-left corners, corresponding to basic states with a relatively shallow reference upper-layer thickness and stronger-than-normal mean winds, the QB mode becomes the most unstable mode and the QQ mode is the second most unstable mode. The lower panels in Fig. 3 show that over the unstable regimes the QQ and QB modes have well-separated periods, with ranges of mostly about 3–6 and 1.5–2.5 yr, respectively.

The boundary between stable and unstable regimes for the QQ and QB modes are marked by the zero growth contours on the plots for the growth rates. The stability boundary of the QB mode is located almost entirely within the unstable regime of the QQ mode.

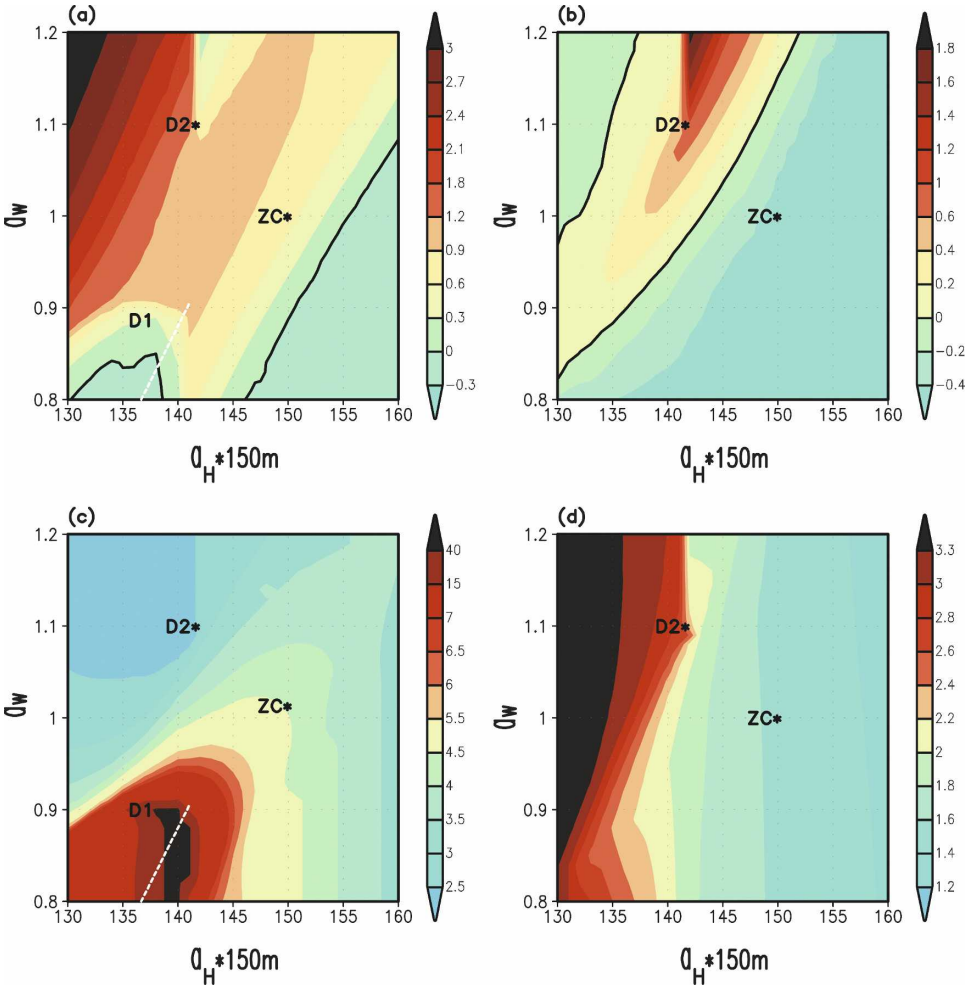

FIG. 4. Same as Fig. 3, but for $\gamma = 0.75$. (a), (c) The qualitative dotted white line denoted by D1 represents a degeneracy of a complex eigenvalue of the QQ mode breaking into double real roots. The point marked by D2 represents a degeneracy of double roots of complex eigenvalues (collapse of the QQ and QB modes). The point marked by ZC represents the point of the standard parameter setting of the original ZC model. (top) The black solid contours correspond to the lines of zero growth rate.

Thus, in the regime above the stability boundary of the QB mode, both QQ and QB are unstable. This coexistence of unstable QQ and QB modes occurs in the regime with climate conditions only modestly different from that of the present climate. This is an important feature that has been overlooked in the earlier theoretical studies by JN93 and FP01.

The stability regime diagrams of QQ and QB modes in Fig. 3 become more complicated when the efficiency factor γ is 0.75, which is the standard value in the ZC model. The most striking feature found in Fig. 4 is the occurrence of two kinds of degeneracy. The first degeneracy occurs over the region marked D1, whereas the second degeneracy occurs at the point marked by D2. D1 consists of a line on which the complex QQ mode breaks down into two real, nonoscillatory modes. The D2 degeneracy consists of the point in the parameter space where the QQ and QB modes collapse into double complex eigenmodes. Near the D2 degeneracy, the QQ and QB modes become extremely sensitive to small changes in the basic state. In fact, these two modes switch regimes. In Fig. 3, the QQ and QB modes coexist but are well separated so that both modes are smooth functions of the basic states. However, in Fig. 4, the QQ and QB modes intersect at D2 and switch their characteristics so that the QQ (QB) mode connects to the QB (QQ) mode.

Away from this pathological point in the parameter space, the coexistence of the QQ and QB modes in Fig. 4 is still similar to what we found in Fig. 3. To wit, in the lower-right quarter of the stability diagrams, characterized by basic states with deeper reference upper-layer thickness and relatively weak winds, both QQ and QB modes are damped. In the middle and toward the upper

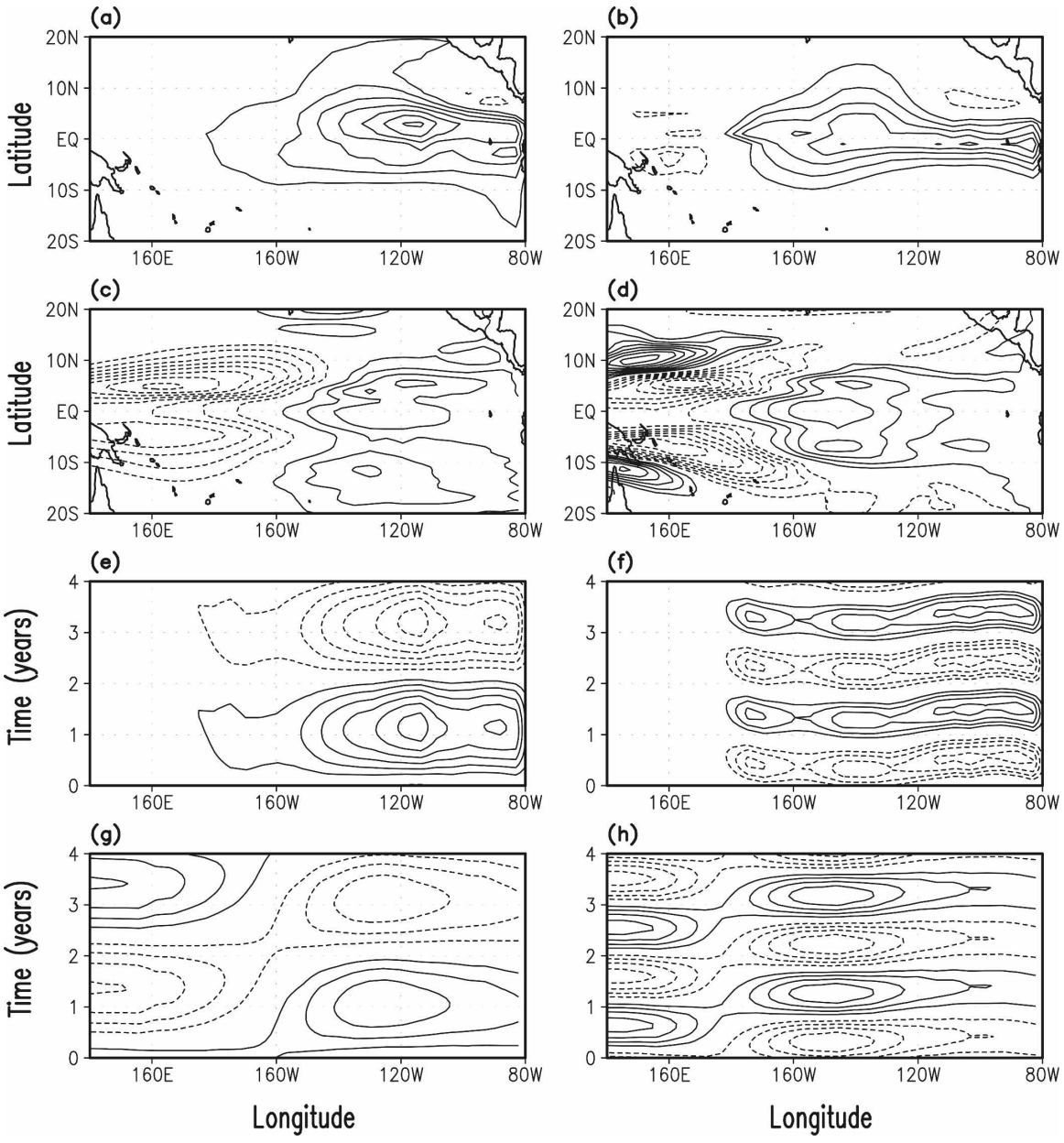

FIG. 5. The leading eigenvectors of the linearized MZC ENSO model. (a), (b) The warm phases of SST anomaly patterns of the QQ and QB modes corresponding to the eigenvalues indicated by the enlarged red squares in Fig. 2c; (c), (d) the corresponding thermocline depth anomaly patterns; (e), (f) the Hovmoeller diagrams along the equator of SST anomaly of the QQ and QB modes; and (g), (h) the corresponding thermocline depth anomaly diagrams. The contour intervals for the SST and thermocline depth panels are 0.5°C and 7.5 m, respectively. Negative value contours are dashed.

part of the regime diagrams, both of these modes are unstable. This regime of the coexistence of QQ and QB modes is still rather broad, although it is less extensive than what is seen in Fig. 3.

b. Eigenstructures of the QQ and QB modes

The typical eigenstructures of the QQ and QB modes are given in Fig. 5. These structures correspond to the eigenmodes denoted by the enlarged red squares in Fig. 2c (a_H = 140/150, a_W = 1, and γ = 0.5). The zonal distributions of the equatorial SST (Figs. 5a,b) and the thermocline patterns (Figs. 5c,d) of these two modes are rather similar, but their meridional structures are significantly different. The QQ mode appears to have a wider meridional extent in the eastern part of the SST pattern and in the western part of the thermocline pat-

tern than the corresponding widths associated with the QB modes.

In terms of the evolution of the equatorial SST and the thermocline depth anomalies, the Hovmoeller diagrams indicate that both the QQ (Figs. 5e,g) and QB (Figs. 5f,h) modes are standing oscillatory modes. The eigenstructure of the QQ is robust in the entire parameter regime, as shown in Fig. 3. However, the eigenstructure of the QB mode undergoes a significant change in its zonal phase propagation when the basic states are in the regime toward the upper-left corner of Fig. 3. In that regime, if we plot the SST field of the QB mode, it has a westward propagation feature (not shown). Thus, the QB mode in this regime becomes similar to the westward-propagating modes found in JN93 and FP01.

c. Comparison with previous studies

The stability regimes found in the earlier studies by JN93 and FP01 suggested that the tropical ocean–atmospheric interaction mainly supports two different kinds of coupled modes—one kind whose nature is tightly related to the ocean dynamics and another whose nature is closely related to the SST thermodynamics. The first kind of mode is marked by a nearly standing oscillation in its equatorial SST evolution, and its dynamics are now understood by either the delay- or recharge-oscillator mechanisms. The second kind of mode has zonal phase propagations in its equatorial SST evolution and it is termed the SST mode (see JN93 for details). The earlier studies also pointed out that these two kinds of modes of different natures may mix into one leading coupled mode. Thus, it was speculated in JN93 and FP01 that the different ENSO behavior observed in nature and simulated in various coupled models may be simply capturing this mixed mode in somehow-different regimes. Clearly, the results in this study point to a different picture. Even in the very neighborhood of the parameter regime centered around the observed basic state, multiple coupled modes, particularly the QQ and QB modes, coexist.

It appears that the reason for which the earlier study by JN93, and the follow-up investigation by FP01, missed this multiplicity of the ENSO-like modes in the coupled model is that it only focused on the most unstable mode. This argument may be inferred from the comparison of the regime diagrams in either Fig. 3 or Fig. 4 with those of FP01's Fig. 4. There are two strong growth-rate regimes over the upper-left and upper-right corners in Fig. 4b in FP01, and in these two regimes the period of the mode falls within the QB and QQ mode ranges, respectively (Fig. 4a in FP01). Similarly, there are two strong growth-rate regimes in similar regions in our Fig. 3—one for the QB mode (the leading mode on the upper-left corner) and one for the QQ mode (the leading mode on the upper-right corner). However, in the two regimes of FP01 there is *one* leading mode that appears to change its nature from one regime to another, whereas in our Fig. 3 and Fig. 4, there are *two* distinct modes, and they take turns as the most unstable mode. If one ignores the lower-left corners in either Fig. 3 or Fig. 4 and overlays the stability regimes of the QQ and QB modes together and then only plots the eigenvalues of the most unstable mode, one roughly gets the same picture as that in Fig. 4 of FP01.

The multiplicity of ENSO modes, largely overlooked so far, provides a different picture of ENSO sensitivity to climate state changes. For instance, there are not only regimes where either the QQ or QB modes dominate, but there is also a regime where both the QQ and QB modes become unstable and coexist. Moreover, the analyses suggest that the regime of coexistence occurs under the present climate conditions (e.g., Jiang et al. 1995). Thus, this coexistence may be responsible for the rich behavior of the observed ENSO variability, such as the occurrences of different types of El Niño (Larkin and Harrison 2005).

5. Heat budget analysis

Heat budget analysis for either observed or simulated SST anomalies is often conducted to diagnose the relative importance of different processes for the ENSO cycles (e.g., Zhang et al. 2007). Here, we carry out a similar heat budget analysis for the eigensolutions of the QQ and QB modes. By comparing the differences in the heat budgets between the QQ and QB modes, we may differentiate the difference of the physical mechanisms for these leading coupled modes.

a. The linear SST tendency equation

The linear SST tendency equation in the MZC model may be written as

$$\frac{\partial T}{\partial t} = -u\frac{\partial \overline{T}}{\partial x} - \overline{u}\frac{\partial T}{\partial x} - v\frac{\partial \overline{T}}{\partial y} - \overline{v}\frac{\partial T}{\partial y} + \gamma\frac{\overline{w}T_{\text{sub}}}{H_1} - w_s\frac{d\overline{T}}{dz} - \left(\alpha_s + \gamma\frac{\overline{w}}{H_1}\right)T. \quad (4)$$

Here, the variables with an overbar refer to climatology monthly mean variables, and the variables without the overbar denote the monthly mean anomaly. The first and the third terms on the right-hand side of Eq. (4) are the advections of the mean SST by the anomalous currents. The second and fourth terms on the right-hand side of Eq. (4) are the advection of the anomalous SST by the mean currents. The fifth term represents the

tendency resulting from the vertical advection of the anomalous subsurface temperature by the mean upwelling. The sixth term is the tendency resulting from the vertical advection of the mean SST by the anomalous upwelling. The final term is the net damping, which is composed of the thermal damping and the damping of the SST anomalies by the mean upwelling. The calculation of each contribution to the SST tendency involves the mean basic state and the corresponding QQ and QB mode eigenvectors.

The mean advection terms $-\overline{u}\partial T/\partial x - \overline{v}\partial T/\partial y - \gamma\overline{w}T/H_1$, and the linear damping $-\alpha_s T$, mainly serve as a damping effect of the SST (Jin et al. 2006). Thus, the phase transition and main positive contributions to the growth of the modes are from upwelling anomalous subsurface temperature anomalies $-\gamma\overline{w}T_{\text{sub}}/H_1$ and the anomalous advection $-u\partial\overline{T}/\partial x - v\partial\overline{T}/\partial x - w_s\partial\overline{T}/\partial z$. Because the term $-v\partial\overline{T}/\partial x$ is always small, the dominating feedback processes for the SST tendency are through the advection of the mean SST by the anomalous zonal flow $-u\partial\overline{T}/\partial x$, and the vertical advection of anomalous subsurface temperature by the mean upwelling $-\gamma\overline{w}T_{\text{sub}}/H_1$, as well as the anomalous upwelling $-w_s\partial\overline{T}/\partial z$. The coupled feedbacks that dominate the SST evolution of the ENSO cycle through these terms are often referred to as the zonal advection, thermocline, and Ekman feedbacks (An and Jin 2001), respectively. In the following sections the spatiotemporal evolutions of these terms are further examined to determine their role in the cycles of the QQ and QB modes.

b. QQ mode evolution

The spatiotemporal evolution of the zonal and vertical advection of the QQ mode, averaged over 2°S–2°N, is shown in Figs. 6a,b, respectively. The month "0" on the *y* axis corresponds to the month at which the maximum SST over the Niño-3 region is reached. Negative (positive) months are before (after) the SST maximum is reached.

The analysis indicates that the thermocline feedback term shown in Fig. 6b is one of the primary factors responsible for the QQ phase transition, which is in agreement with the recharge-oscillator theory. For instance, at 12 months prior to the peak warm phase of the QQ mode, the thermocline feedback already contributes to the initiation of the warming, whereas 12 months after the peak warm phase, this term gives rise to a cooling tendency.

The heat budget analysis also shows that the advection of the mean SST by the anomalous zonal flow (Fig. 6a) is important in the equatorial central and eastern Pacific from 150° to 100°W. It tends to peak about 10 months before (after) the peak warm (cold) phase, when the QQ mode cycle is at its transition phase. These results are entirely consistent with the revised version of the recharge-oscillator model (Jin and An 1999).

The four phases of the cycle of the model-simulated QQ mode can be described by Fig. 7. Phases I and III represent the warm and cold phases, respectively. Phases IV and II are El Niño and La Niña on set phases. Prior to El Niño (the aftermath of a cold phase), upper-ocean heat content or warm water volume over the entire tropical Pacific tends to build up gradually; therefore, subsurface ocean temperature in the main thermocline is weakly warmer than normal along the entire equatorial region (lower panel in phase IV). This recharged state is the consequence of the recharge process indicated by the arrows of ocean currents in the lower panel of phase III. The transition phase IV is characterized by three important features: a weakly deeper-than-normal equatorial thermocline, eastward ocean current anomalies, which can be inferred from the geostrophic balance, and the disappearance of surface temperature anomalies and their associated equatorial wind anomalies. The vertical advection of anomalously warm subsurface temperature by the mean upwelling and the advection of the mean SST by the anomalous zonal flow provide the positive SST tendency to generate the positive SST anomalies and initiate the warm phase, as shown in phase I of Fig. 7. These positive SST anomalies generate westerly wind anomalies, which redistribute the subsurface ocean heat content, such that the thermocline depth shoals in the warm pool region and deepens in the cold tongue region. This process gives rise to cold and warm subsurface temperature anomalies in the western and eastern Pacific, respectively. The SST anomalies are intensified by the anomalous vertical advection of even warmer subsurface temperature anomalies to the surface by the mean upwelling. The discharge of the equatorial heat content during the warm phase, which is indicated by the arrows in the lower panel in phase I, is the mechanism that eventually turns this phase around. The continuous discharge of the equatorial heat content, resulting from the wind-forced redistribution of the subsurface ocean heat content, not only leads to the demise of the warm phase, but also leads a cold equatorial subsurface temperature anomaly in the entire tropical Pacific, as indicated in the lower panel in phase II. The cold equatorial subsurface temperature anomalies are accompanied by westward zonal current anomalies (geostrophic current anomalies). The vertical advection of the anomalous subsurface temperature by the mean upwelling and the advection of the mean SST by the anomalous zonal flow provide the negative

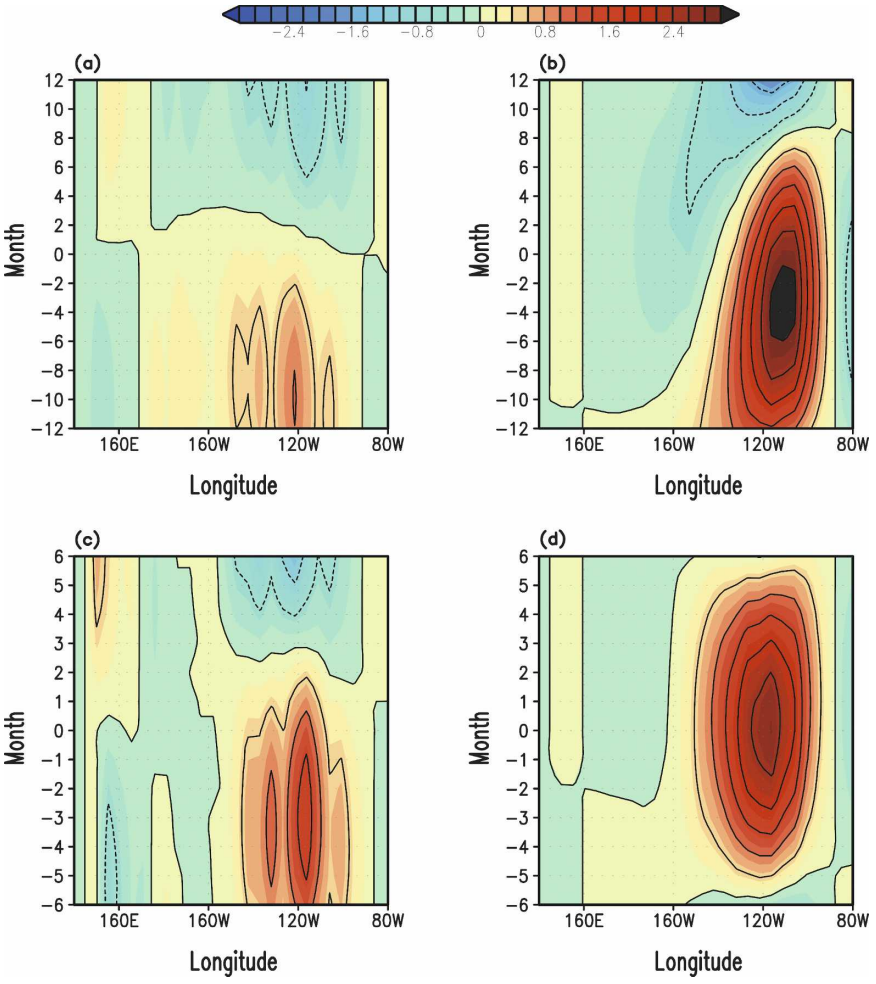

FIG. 6. Hovmoeller diagrams of the (a) zonal ($-u\partial\overline{T}/\partial x$) and (b) vertical ($\gamma\overline{w}T_{\text{sub}}/H_1$) advections of the QQ mode. The month "0" on the y axis corresponds to the month at which the maximum SST over the Niño-3 region is reached. Negative (positive) months are before (after) the SST maximum; 0.5°C yr^{-1} contours are overlaid. (c), (d) Same as (a), (b), respectively, but for the QB mode.

SST tendency to generate the negative SST anomalies and initiate the cold phase QQ mode cycle. These results are entirely consistent with those by Zhang et al. (2007) who analyzed the net surface heat flux of the ENSO cycle simulated by the National Centers for Environmental Prediction (NCEP) coupled forecast model, which has an ENSO cycle of about 5 yr.

c. QB mode evolution

The spatiotemporal evolution of the zonal and vertical advections of the QB mode (Figs. 6c,d) indicates that the vertical advection of anomalous subsurface temperature by the mean upwelling (Fig. 6d) is again the main positive feedback used to overcome the total damping, becausee it reaches its maximum strength around month "0," at the peak of the warm phase of the QB mode cycle.

A comparison between Figs. 6a,b indicates that the advection of the mean SST by the anomalous zonal flow in the QB mode is at least twice as large as that in the QQ mode. Fig. 6a also indicates that this term is the main physical process responsible for the phase transition of the QB mode. This advective feedback reaches its maximum intensity around 3 months prior to the peak warm phase, and 3 months after the peak it gives rise to a cooling tendency.

The cycle of the model-simulated QB mode can be seen in Fig. 8. During the warm phase, the easterly equatorial winds over the eastern Pacific and westerly equatorial winds over the central Pacific (associated with the maximum SST anomalies at about 140°W) re-

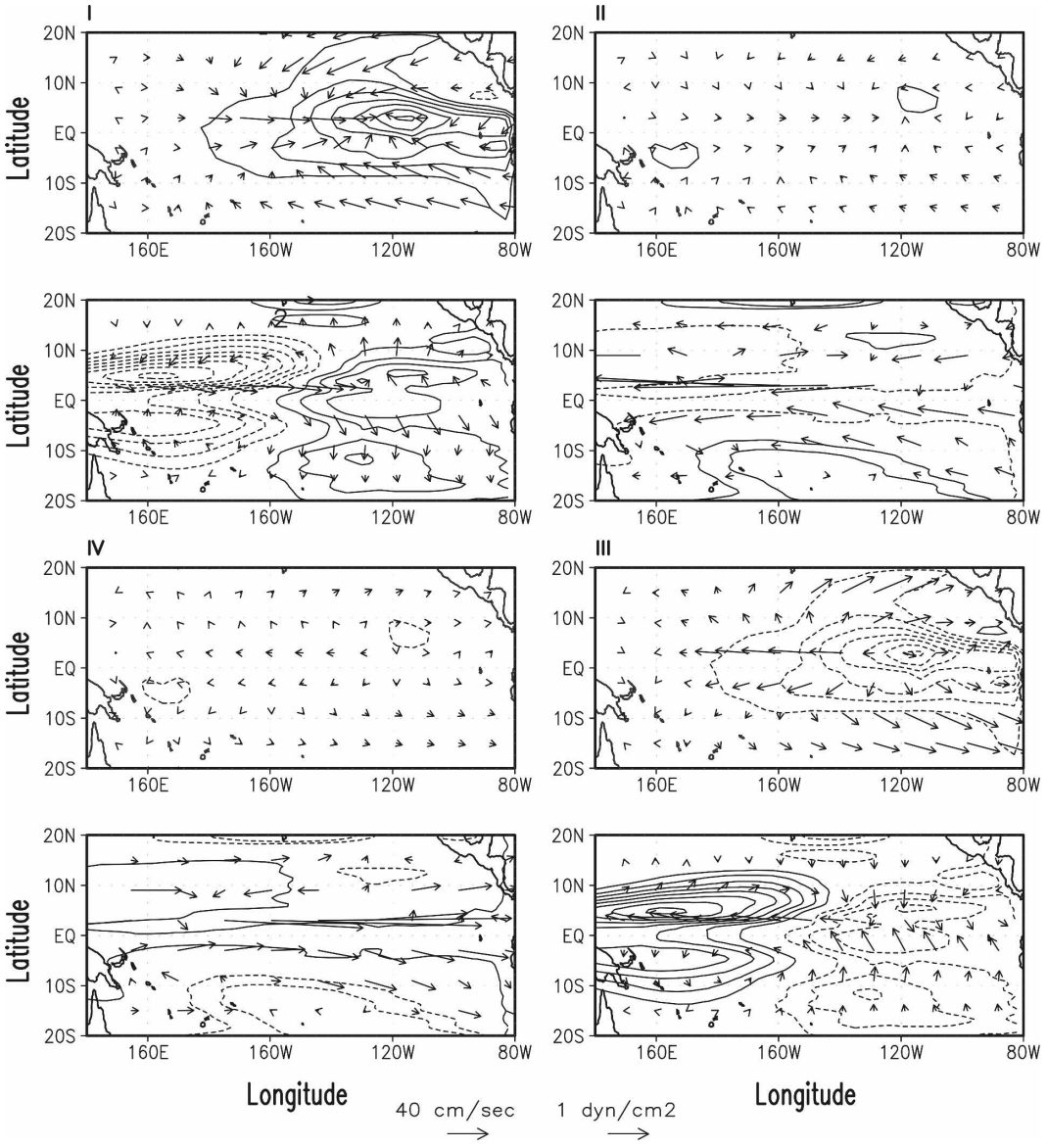

FIG. 7. Eigenvector fields of the QQ mode illustrating the QQ mode cycle: I and III represent the warm and cold phases, respectively, and II and IV are the transition phases. Each phase is described by two panels: (top) the SST (contours) and wind stress (arrows), and (bottom) the thermocline depth (contours) and wave-induced current (arrows). The contour intervals for the SST and thermocline depth are 0.5°C and 7.5 m, respectively, and the scales for the ocean current (cm s^{-1}) and the wind stress (dyn cm^{-2}) are given by the arrows located at the bottom of the figure.

sult in convergence of the wind in this region (upper panel in phase I). Unlike the QQ mode, in which the wave-induced equatorial currents are a significant meridional component for the discharge of the heat content, in the QB mode, the westward zonal currents anomalies dominate, as is seen in the lower panel of phase I. These westward zonal currents in the equatorial band, which are associated with both upwelling Kelvin and downwelling Rossby waves, are the primary factor responsible for the QB phase transition (phase II). The westward zonal currents give rise to a cold SST advection over the eastern and central Pacific, which turns around the warm phase. The converse occurs during the cold phase. The results suggest that the main phase transition mechanism for the QB mode is through the zonal advection feedback, which was emphasized in the reflective–advective oscillator proposed by Picaut et al. (1997).

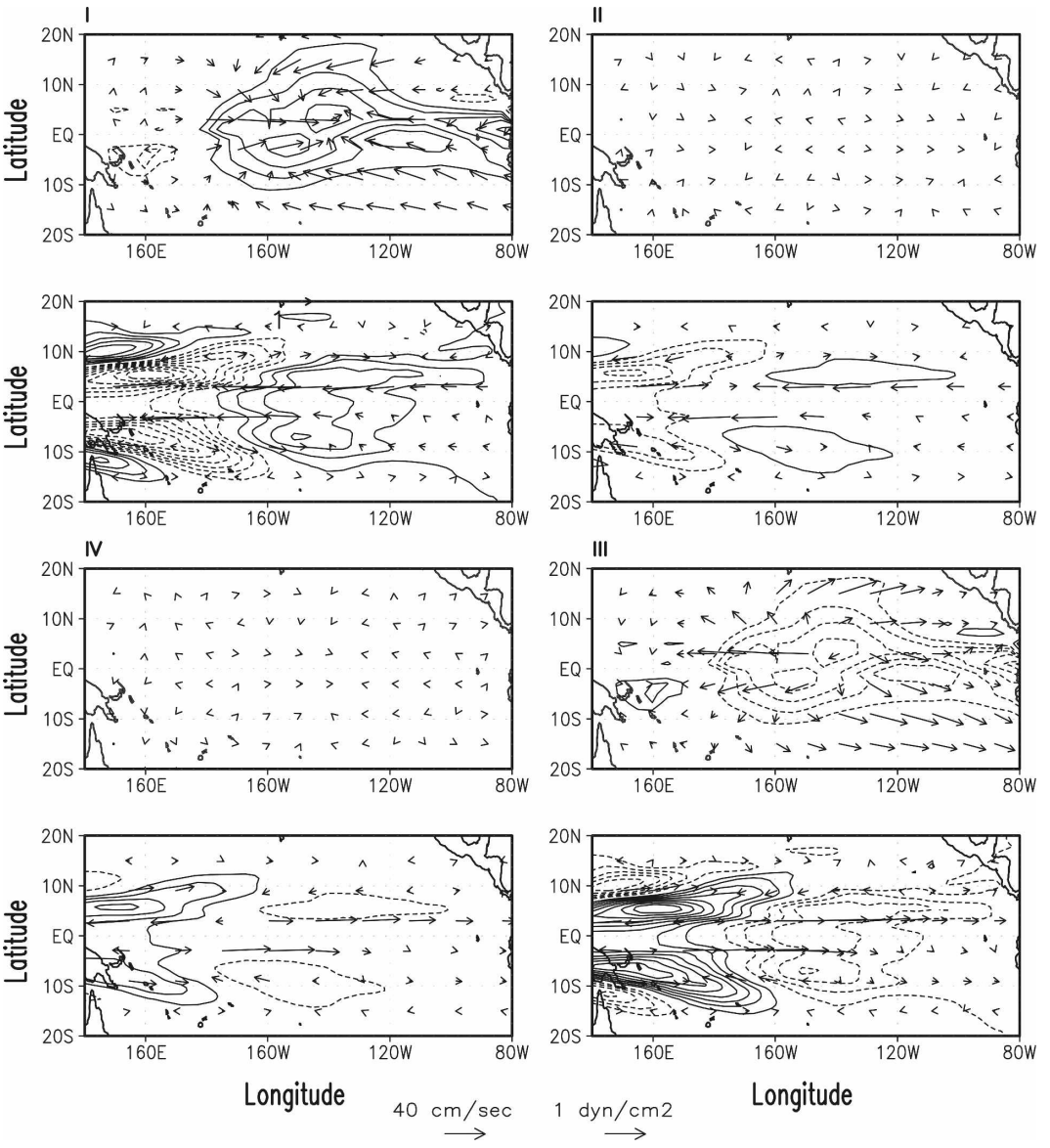

FIG. 8. Same as Fig. 7, but for the QB mode.

The Ekman feedback through the anomalous upwelling $-w_s\partial\overline{T}/\partial z$ is of less importance for either the QQ or QB modes. However, it becomes a dominating process for the SST field of a third coupled mode (Bejarano 2006) that has a period about 10–15 months. This mode is heavily damped in the parameter regimes analyzed in Figs. 3 and 4. It becomes a leading mode when the parameter γ is further reduced and may also mix with the QB mode (Bejarano 2006).

6. Nonlinear regimes

A large number of nonlinear integrations of the MZC ENSO model have been performed in four different regimes of the stability diagrams (Fig. 3) to explore the nonlinear behaviors of the QQ and QB modes. These four regimes are as follows: (i) the QQ regime, where the QQ mode is unstable and the QB mode is stable; (ii) the QQ and QB regime, where both QQ and QB modes are unstable; (iii) the QB regime, where the QB mode is the most unstable mode; and (iv) the stable regime, where both QQ and QB modes are stable. After prescribing the regime, the MZC model is run freely for 100 yr. To be consistent with the eigenanalysis, the seasonal cycle of the basic state has been omitted in these nonlinear integrations. In other words, the runs are performed by using the annual mean basic state only.

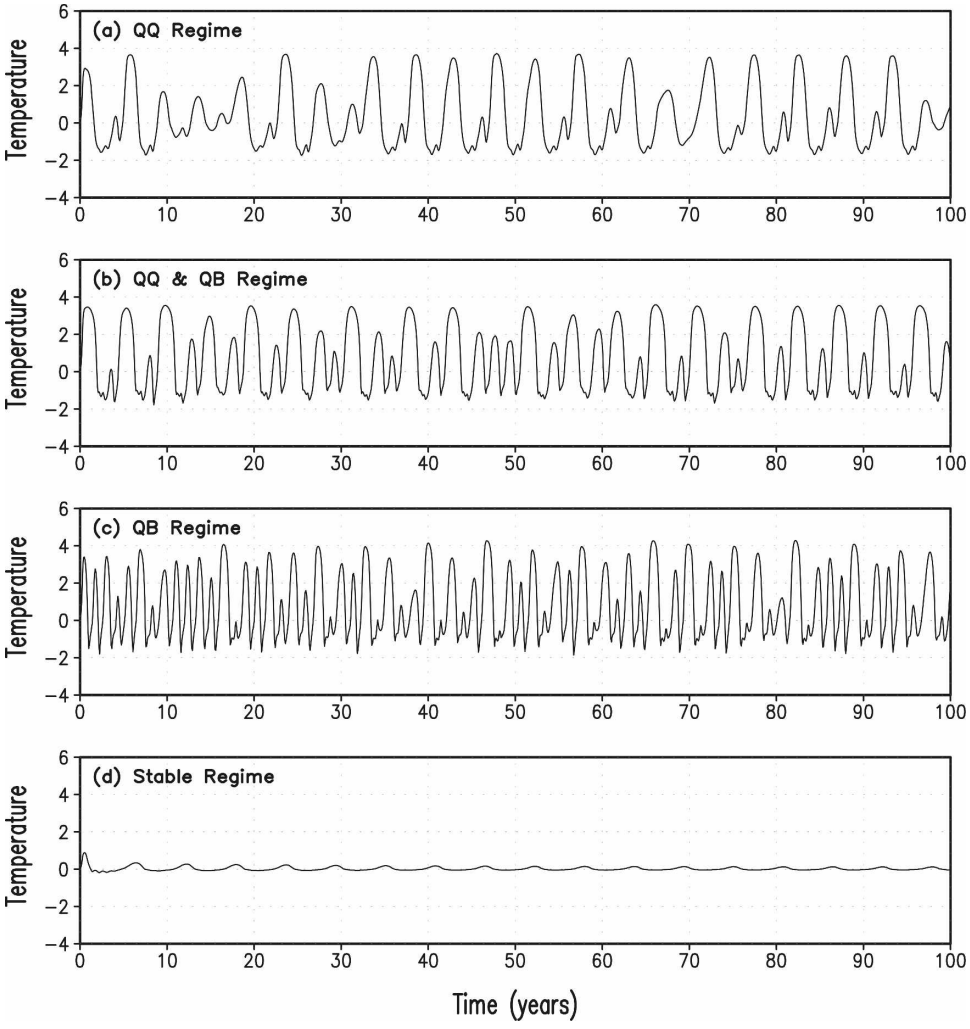

FIG. 9. Time series of the Niño-3 SST anomaly (°C) calculated by nonlinear integration of the MZC model (a) in an unstable QQ parameter regime ($a_H = 1,\ a_W = 1$), (b) in an unstable QQ and QB parameter regime ($a_H = 145/150,\ a_W = 1$), (c) in an unstable QB parameter regime ($a_H = 140/150$, $a_W = 1.2$), and (d) in a stable QQ and QB parameter regime ($a_H = 1,\ a_W = 0.9$).

The characteristic variability in each of the four different regimes is summarized in time-versus-amplitude plots of the SST anomaly over the Niño 3 region (Fig. 9). The ENSO evolution in the unstable QQ regime is drastically different from that in the unstable QQ and QB regime, as illustrated in Figs. 9a,b. In the QQ regime, the ENSO evolution is dominated by weakly chaotic QQ cycles. For the case shown in this figure, the spectrum of the time series of Niño-3 in this regime shows a clean peak with a period of 60 months (Fig. 10a). In the QQ and QB regime, the ENSO evolution becomes much more erratic with both QQ and QB cycles (Fig. 9b). The coexistence of both modes is clearly indicated by the presence of 28- and 60-month peaks in the spectral analysis of the modeled QQ and QB regime time series (Fig. 10b). Because both oscillatory modes are unstable in the QQ and QB regime, nonlinear interactions between the modes may exhibit chaotic behavior with a high level of intermittence. This chaotic behavior is different from the chaos scenario found by Jin et al. (1994) and Tziperman et al. (1994), where they emphasize the role of the nonlinear interactions between an ENSO mode and the annual cycle in the basic state. The nonlinear integrations in the QB regime, which are characteristically in the upper-left corners of the stability diagrams, exhibit 1.5–2.0-yr ENSO events (Fig. 9c). Although the QB peak dominates (Fig. 10c), the presence of a secondary peak with QQ periodicity is also observed. The nonlinear integrations over stable regimes indicate that the oscillatory modes are damped (Fig. 9d). Although nonlinearity is clearly important for generating complex behavior, the

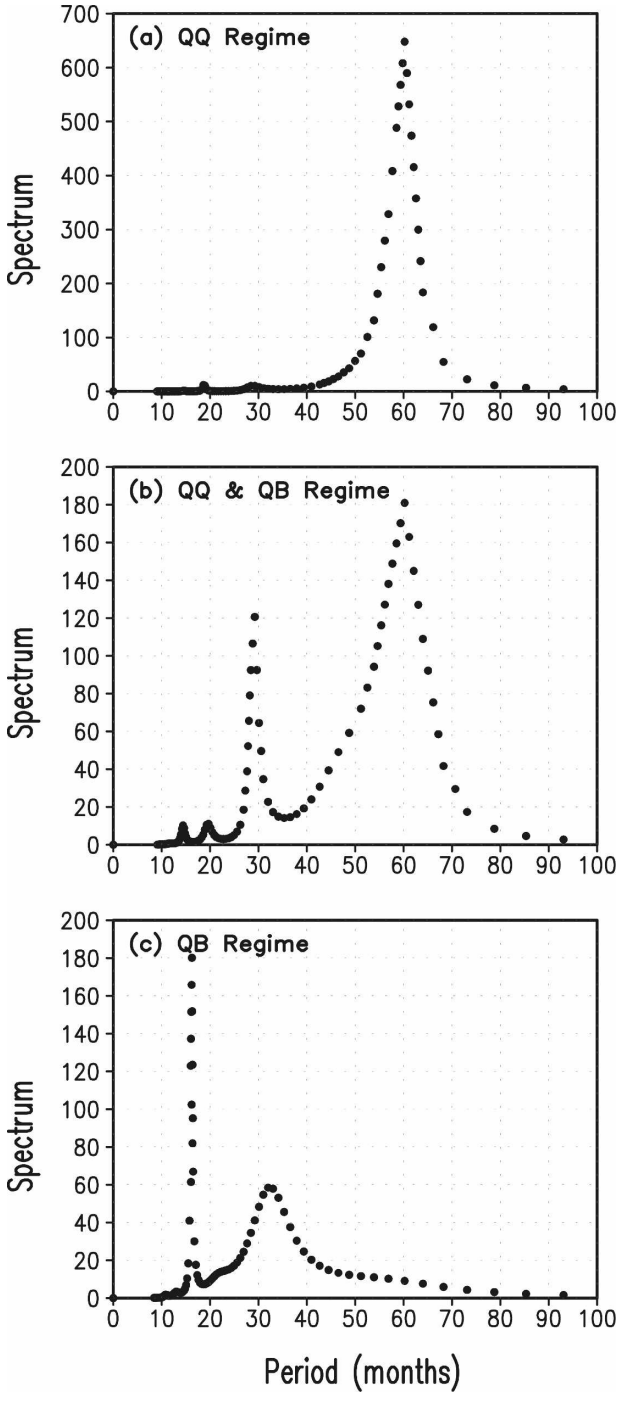

FIG. 10. The spectra corresponding to the time series of the cases in Figs. 9a–c (a) in an unstable QQ parameter regime, (b) in an unstable QQ and QB parameter regime, and (c) in an unstable QB parameter regime.

linear eigenanalysis provides quantitative information about the dominance of a particular leading mode in the different regimes.

The results indicate that in regimes (i)–(iii), the unstable modes emerge and become sustained oscillations without stochastic forcing, whereas the stable modes in regime (iv) can only be sustained by stochastic forcing. The possible excitations of the QQ and QB modes by stochastic forcing will be pursued in future studies.

7. Conclusions

In this study, we illustrate that the ocean–atmosphere interactions in the Tropics can yield at least two types of independent modes: a low- (QQ) and a higher-frequency (QB) mode. Under climate conditions that are not significantly different from those of the present climate, the MZC model has found at least two unstable modes to coexist. This multiplicity of the ENSO mode is a robust feature of the coupled system.

The heat budget analysis shows that the QQ mode is characterized by a dominance of the thermocline feedback, which not only serves as the main positive feedback that overcomes the damping effects, but is also the main process responsible for the QQ phase transition. These vertical movements of the thermocline that produce the dominant effect on the SST are determined by the ocean mass adjustment to the winds in the equatorial region. The QQ mode is clearly a "recharge oscillator" mode. The analysis also suggests that the advective feedback is the most important phase transition mechanism in the QB mode, while the role of the thermocline feedback is mainly to overcome the negative feedback of the damping terms. This mode behaves, to some extent, as the advective–reflective oscillator.

Our study is in contrast with earlier studies by Jin and Neelin (1993a) and by FP01. In these earlier studies, the focus is on the first leading mode. The leading mode was perceived to change its nature smoothly from a recharge-oscillator-type mode to an SST mode from one part of the parameter regime to another, and its frequency also changes smoothly from one regime to another. In the current study, it has been demonstrated that, in fact, there are two kinds of coupled modes with distinct periodicities, although each may dominate in different regimes.

The stability diagrams indicate that the QQ mode tends to become stable for basic states with either very shallow or very deep reference upper-layer thickness. If the thermocline is too deep, its vertical displacements have little impact on the SST, so the thermocline feedback, which is responsible for the maintenance of the QQ mode, is suppressed. On the other hand, if the reference upper-layer thickness is too shallow, the mean SST over the eastern Pacific decreases (Fig. 1), which reduces the vertical temperature gradients and stabilizes the QQ mode. It is important to note that

shoaling the reference upper-layer thickness has another effect; it increases the east–west temperature gradient, which favors the QB mode, which tends to be the dominating mode in the regime with shallow upper-layer thickness and strong mean winds.

Comparison between the linear eigenanalysis and the nonlinear integrations shows that the qualitative natures of the nonlinear solutions are captured by the linear modes. Some of the nonlinear behavior of ENSO, such as significant intermittency in the unstable QQ and QB regime, may have relevance to the observed ENSO evolutions. Strong ENSO events, such as those observed in 1982/83 and 1997/98, burst out with irregular intervals and relatively weak ENSO activity in between these intervals. In the past decade, the debate regarding the main sources of ENSO irregularity shifted from blaming low-order deterministic chaos (e.g., Jin et al. 1994; Tziperman et al. 1994; Chang et al. 1994) to faulting random disturbances that agitate the otherwise damped ENSO modes (Penland and Sardeshmukh 1995; Chang et al. 1996; Thompson and Battisti 2001). Thus, it is plausible that the coexistence of the QQ and QB modes may contribute to observed rich variations in ENSO (Larkin and Harrison 2005).

Finally, it is our conjecture that the QQ and QB modes of ENSO contribute to the ubiquitous QB variability of the tropical climate. It is plausible that the strong QB signal observed in signals associated with the monsoon may involve amplification of the impact of this QB mode of ENSO through local dynamical processes (e.g., Meehl 1994, 1997; Kim and Lau 2001; Li et al. 2001) that are important in monsoon systems.

Acknowledgments. This research is supported by NOAA Grant GC01-229, NSF Grants ATM0226141 and ATM0424799, and National Natural Science Foundation of China (NSFC) Grant 40528006. The authors thank Drs. Ming Cai, S.-I. An, and A. Timmerman for stimulating discussions, and Dr. A. Barcilon for editing the manuscript.

REFERENCES

An, S.-I., and F.-F. Jin, 2001: Collective role of thermocline and zonal advective feedbacks in the ENSO mode. *J. Climate,* **14,** 3421–3432.

Barnett, T. P., D. W. Pierce, M. Latif, D. Dommenget, and R. Saravanan, 1999: Interdecadal interactions between the tropics and midlatitudes in the Pacific basin. *Geophys. Res. Lett.,* **26,** 615–618.

Battisti, D. S., 1988: Dynamics and thermodynamics of a warming event in a coupled tropical atmosphere–ocean model. *J. Atmos. Sci.,* **45,** 2889–2919.

——, and A. C. Hirst, 1989: Interannual variability in a tropical atmosphere–ocean model: Influence of the basic state, ocean geometry, and nonlinearity. *J. Atmos. Sci.,* **46,** 1687–1712.

Bejarano, L. F., 2006: Coexistence of leading equatorial coupled modes for ENSO. Ph.D. thesis, The Florida State University, 118 pp.

Bjerknes, J., 1969: Atmospheric teleconnections from the equatorial Pacific. *Mon. Wea. Rev.,* **97,** 163–172.

Cane, M. A., 1984: Modeling sea level during El Niño. *J. Phys. Oceanogr.,* **14,** 1864–1874.

——, and S. E. Zebiak, 1985: A theory for El Niño and the Southern Oscillation. *Science,* **228,** 1085–1087.

Chang, P., B. Wang, T. Li, and L. Ji, 1994: Interactions between the seasonal cycle and the Southern Oscillation-frequency entrainment and chaos in a coupled ocean-atmosphere model. *Geophys. Res. Lett.,* **21,** 2817–2820.

——, L. Ji, H. Li, and M. Flügel, 1996: Chaotic dynamics versus stochastic processes in El Niño-Southern Oscillation in coupled ocean-atmosphere models. *Physica D,* **98,** 301–320.

Deser, C., and M. L. Blackmon, 1995: On the relationship between tropical and North Pacific sea surface temperature variations. *J. Climate,* **8,** 1677–1680.

——, M. A. Alexander, and M. S. Timlin, 1996: Upper-ocean thermal variations in the North Pacific during 1970–1991. *J. Climate,* **9,** 1840–1855.

Fedorov, A. V., and S. G. Philander, 2000: Is El Niño changing? *Science,* **288,** 1997–2002.

——, and ——, 2001: A stability analysis of tropical ocean–atmosphere interactions: Bridging measurements and theory for El Niño. *J. Climate,* **14,** 3086–3101.

Gill, A. E., 1980: Some simple solutions for heat-induced tropical circulation. *Quart. J. Roy. Meteor. Soc.,* **106,** 447–462.

Gu, D., and S. G. H. Philander, 1997: Interdecadal climate fluctuations that depend on exchanges between the tropics and extratropics. *Science,* **275,** 805–807.

Hirst, A. C., 1986: Unstable and damped equatorial modes in simple coupled ocean–atmosphere models. *J. Atmos. Sci.,* **43,** 606–630.

Jiang, N., J. D. Neelin, and M. Ghil, 1995: Quasi-quadrennial and quasi-biennial variability in COADS equatorial Pacific sea surface temperature and winds. *Climate Dyn.,* **12,** 101–112.

Jin, F.-F., 1996: Tropical ocean-atmosphere interaction, the Pacific cold tongue, and the El Niño-Southern Oscillation. *Science,* **274,** 76–78.

——, 1997a: An equatorial ocean recharge paradigm for ENSO. Part I: Conceptual model. *J. Atmos. Sci.,* **54,** 811–829.

——, 1997b: An equatorial ocean recharge paradigm for ENSO. Part II: A stripped-down coupled model. *J. Atmos. Sci.,* **54,** 830–847.

——, 1997c: A theory of interdecadal climate variability of the North Pacific ocean-atmosphere system. *J. Climate,* **10,** 1821–1835.

——, 2001: Low-frequency modes of tropical ocean dynamics. *J. Climate,* **14,** 3874–3881.

——, and J. D. Neelin, 1993a: Modes of interannual tropical ocean-atmosphere interaction—A unified view. Part I: Numerical results. *J. Atmos. Sci.,* **50,** 3477–3503.

——, and ——, 1993b: Modes of interannual tropical ocean-atmosphere interaction—A unified view. Part III: Analytical results in fully coupled cases. *J. Atmos. Sci.,* **50,** 3523–3540.

——, and S.-I. An, 1999: Thermocline and zonal advective feedbacks within the equatorial ocean recharge oscillator model for ENSO. *Geophys. Res. Lett.,* **26,** 2989–2992.

——, J. D. Neelin, and M. Ghil, 1994: El Niño on the devil's

staircase: Annual subharmonic steps to chaos. *Science,* **264,** 70–72.

——, M. Kimoto, and X. C. Wang, 2001: A model of decadal ocean–atmosphere interaction in the North Pacific basin. *Geophys. Res. Lett.,* **28,** 1531–1534.

——, J.-S. Kug, S.-I. An, and I.-S. Kang, 2003: A near-annual coupled ocean–atmosphere mode in the equatorial Pacific ocean. *Geophys. Res. Lett.,* **30,** 1080, doi:10.1029/2002GL015983.

——, S. T. Kim, and L. Bejarano, 2006: A coupled-stability index for ENSO. *Geophys. Res. Lett.,* **33,** L23708, doi:10.1029/2006GL027221.

Kim, K.-M., and K.-M. Lau, 2001: Dynamics of monsoon-induced biennial variability in ENSO. *Geophys. Res. Lett.,* **28,** 315–318.

Kleeman, R., J. P. McCreary, and B. A. Klinger, 1999: A mechanism for generating ENSO decadal variability. *Geophys. Res. Lett.,* **26,** 1743–1746.

Larkin, N. K., and D. E. Harrison, 2005: Global seasonal temperature and precipitation anomalies during El Niño autumn and winter. *Geophys. Res. Lett.,* **32,** L16705, doi:10.1029/2005GL022860.

Latif, M., 1998: Dynamics of interdecadal variability in coupled ocean–atmosphere models. *J. Climate,* **11,** 602–624.

——, and T. P. Barnett, 1994: Causes of decadal climate variability over the North Pacific/North American sector. *Science,* **266,** 634–637.

Li, T., C.-W. Tham, and C.-P. Chang, 2001: A coupled air–sea–monsoon oscillator for the tropospheric biennial oscillation. *J. Climate,* **14,** 752–764.

McPhaden, M. J., and Coauthors, 1998: The Tropical Ocean-Global Atmosphere observing system: A decade of progress. *J. Geophys. Res.,* **103,** 14 169–14 240.

Meehl, G. A., 1994: Coupled land-ocean-atmosphere processes and south Asian monsoon variability. *Science,* **266,** 263–267.

——, 1997: The south Asian monsoon and the tropospheric biennial oscillation. *J. Climate,* **10,** 1921–1943.

Miller, A. J., D. R. Cayan, and W. B. White, 1998: A westward-intensified decadal change in the North Pacific thermocline and gyre-scale circulation. *J. Climate,* **11,** 3112–3127.

Neelin, J. D., 1990: A hybrid coupled general circulation model for El Niño studies. *J. Atmos. Sci.,* **47,** 674–693.

——, and F.-F. Jin, 1993: Modes of interannual tropical ocean–atmosphere interaction—a unified view. Part II: Analytical results in the weak coupling limit. *J. Atmos. Sci.,* **50,** 3504–3522.

——, M. Latif, and F.-F. Jin, 1994: Dynamics of coupled ocean-atmosphere models: The tropical problem. *Annu. Rev. Fluid Mech.,* **26,** 617–659.

——, D. S. Battisti, A. C. Hirst, F.-F. Jin, Y. Wakata, T. Yamagata, and S. E. Zebiak, 1998: ENSO theory. *J. Geophys. Res.,* **103,** 14 261–14 290.

Penland, C., and P. D. Sardeshmukh, 1995: The optimal growth of tropical sea surface temperature anomalies. *J. Climate,* **8,** 1999–2024.

Perigaud, C., and B. Dewitte, 1996: El Niño–La Niña events simulated with Cane and Zebiak's model and observed with satellite or in situ data. Part I: Model data comparison. *J. Climate,* **9,** 66–84.

Philander, S. G. H., 1990: *El Niño, La Niña, and the Southern Oscillation.* Academic Press, 293 pp.

——, T. Yamagata, and R. C. Pacanowski, 1984: Unstable air–sea interactions in the tropics. *J. Atmos. Sci.,* **41,** 604–613.

——, R. C. Pacanowski, N.-C. Lau, and M. J. Nath, 1992: Simulation of ENSO with a global atmospheric GCM coupled to a high-resolution, tropical Pacific Ocean GCM. *J. Climate,* **5,** 308–329.

Picaut, J., F. Masia, and Y. du Penhoat, 1997: An advective-reflective conceptual model for the oscillatory nature of ENSO. *Science,* **277,** 663–666.

Rasmusson, E. M., and T. H. Carpenter, 1982: Variations in tropical sea surface temperature and surface wind fields associated with the Southern Oscillation/El Niño. *Mon. Wea. Rev.,* **110,** 354–384.

Schneider, N., 2000: A decadal spiciness mode in the tropics. *Geophys. Res. Lett.,* **27,** 257–260.

Schopf, P. S., and M. J. Suarez, 1988: Vacillations in a coupled ocean–atmosphere model. *J. Atmos. Sci.,* **45,** 549–566.

Suarez, M. J., and P. S. Schopf, 1988: A delayed action oscillator for ENSO. *J. Atmos. Sci.,* **45,** 3283–3287.

Thompson, C. J., and D. S. Battisti, 2001: A linear stochastic dynamical model of ENSO. Part II: Analysis. *J. Climate,* **14,** 445–466.

Tozuka, T., and T. Yamagata, 2003: Annual ENSO. *J. Phys. Oceanogr.,* **33,** 1564–1578.

Trenberth, K. E., and J. W. Hurrell, 1994: Decadal atmosphere-ocean variations in the Pacific. *Climate Dyn.,* **9,** 303–319.

Tziperman, E., L. Stone, H. Jarosh, and M. A. Cane, 1994: El Niño chaos: Overlapping of resonances between the seasonal cycle and the Pacific ocean-atmosphere oscillator. *Science,* **264,** 72–74.

Wallace, J. M., E. M. Rasmusson, T. P. Mitchell, V. E. Kousky, E. S. Sarachik, and H. von Storch, 1998: On the structure and evolution of ENSO-related climate variability in the tropical Pacific: Lessons from TOGA. *J. Geophys. Res.,* **103,** 14 241–14 260.

Wang, C., and J. Picaut, 2004: Understanding ENSO physics—A review. *Earth's Climate: The Ocean–Atmosphere Interaction, Geophys. Monogr.,* Vol. 147, Amer. Geophys. Union, 21–48.

Wang, X., F.-F. Jin, and Y. Wang, 2003a: A tropical ocean recharge mechanism for climate variability. Part I: Equatorial heat content changes induced by the off-equatorial wind. *J. Climate,* **16,** 3585–3598.

——, ——, and ——, 2003b: A tropical ocean recharge mechanism for climate variability. Part II: A unified theory for decadal and ENSO modes. *J. Climate,* **16,** 3599–3616.

Weisberg, R. H., and C. Wang, 1997: A western Pacific oscillator paradigm for the El Niño-Southern Oscillation. *Geophys. Res. Lett.,* **24,** 779–782.

Zebiak, S. E., 1984: Tropical atmosphere-ocean interaction and the El Niño-Southern Oscillation phenomenon. Ph.D. dissertation, Massachusetts Institute of Technology, 261 pp.

——, and M. A. Cane, 1987: A model El Niño–Southern Oscillation. *Mon. Wea. Rev.,* **115,** 2262–2278.

Zhang, Q., A. Kumar, Y. Xue, W. Wang, and F. F. Jin, 2007: Analysis of the ENSO cycle in the NCEP coupled forecast model. *J. Climate,* **20,** 1265–1284.

Zhang, Y., J. M. Wallace, and D. S. Battisti, 1997: ENSO-like interdecadal variability: 1900–93. *J. Climate,* **10,** 1004–1020.